



Effect of temperature and rhenium content in precipitates on dispersion hardening of tungsten

Yulia R. Sharapova

Research Laboratory for Metals and Alloys under Extreme Impacts, Ufa University of Science and Technology, Ufa, Russia;

Arseny M. Kazakov

Research Laboratory for Metals and Alloys under Extreme Impacts, Ufa University of Science and Technology, Ufa, Russia;; arseny.m.kazakov@gmail.com

Elena A. Korznikova

Research Laboratory for Metals and Alloys under Extreme Impacts, Ufa University of Science and Technology, Ufa, Russia

Alexandr Zinovev

Institute for Nuclear Materials Science, SCK CEN, Mol, Belgium;

Dmitry Terentyev

Institute for Nuclear Materials Science, SCK CEN, Mol, Belgium;

See next page for additional authors

Follow this and additional works at: <https://kijoms.uokerbala.edu.iq/home>



Part of the [Atomic, Molecular and Optical Physics Commons](#), [Computer Sciences Commons](#), [Condensed Matter Physics Commons](#), and the [Nuclear Commons](#)

Recommended Citation

Sharapova, Yulia R.; Kazakov, Arseny M.; Korznikova, Elena A.; Zinovev, Alexandr; Terentyev, Dmitry; and Dmitriev, Sergey V. (2024) "Effect of temperature and rhenium content in precipitates on dispersion hardening of tungsten," *Karbala International Journal of Modern Science*: Vol. 11 : Iss. 1 , Article 3.

Available at: <https://doi.org/10.33640/2405-609X.3386>

This Research Paper is brought to you for free and open access by Karbala International Journal of Modern Science. It has been accepted for inclusion in Karbala International Journal of Modern Science by an authorized editor of Karbala International Journal of Modern Science. For more information, please contact abdulateef1962@gmail.com.



Effect of temperature and rhenium content in precipitates on dispersion hardening of tungsten

Abstract

Tungsten (W) is being developed as a plasma-facing material for fusion reactors, where it is subjected to MeV neutron irradiation, low-energy helium isotope particles, and high temperatures. These conditions lead to the formation of point defects, dislocation loops, voids, and transmutation into rhenium (Re) and osmium (Os), which form precipitates that significantly impact dislocation motion and increase hardness. This study uses molecular dynamics modeling to examine the interaction between an edge dislocation and Re-rich particles of various stoichiometries, specifically coherent bcc-phase particles and noncoherent σ -phase precipitates. Results show that shear stress increases by approximately 20-40% with larger particle size (3-5 nm diameter) and higher Re content (50-75 at.%), while temperature (600–1400 K) has a weak effect on critical shear stress. Coherent bcc-phase particles are weak barriers to dislocations, whereas noncoherent σ -phase precipitates are strong obstacles. The study reveals that dislocations typically cut through these particles, except for noncoherent spherical ones, which are bypassed via the Orowan mechanism.

Keywords

tungsten; molecular dynamics method; dispersion hardening; deformation; dislocation

Creative Commons License



This work is licensed under a [Creative Commons Attribution-Noncommercial-No Derivative Works 4.0 License](https://creativecommons.org/licenses/by-nc-nd/4.0/).

Authors

Yulia R. Sharapova, Arseny M. Kazakov, Elena A. Korznikova, Alexandr Zinovev, Dmitry Terentyev, and Sergey V. Dmitriev

RESEARCH PAPER

Effect of Temperature and Rhenium Content in Precipitates on Dispersion Hardening of Tungsten

Yulia R. Sharapova^a, Arseny M. Kazakov^{a,*}, Elena A. Korznikova^{a,b}, Alexandr Zinovev^c, Dmitry Terentyev^c, Sergey V. Dmitriev^d

^a Research Laboratory for Metals and Alloys under Extreme Impacts, Ufa University of Science and Technology, Ufa, Russia

^b Polytechnic Institute (Branch) in Mirny, North-Eastern Federal University, Mirny, Russia

^c Institute for Nuclear Materials Science, SCK CEN, Mol, Belgium

^d Institute of Molecule and Crystal Physics, UFRC of Russian Academy of Sciences, Ufa, Russia

Abstract

Tungsten (W) is being developed as a plasma-facing material for fusion reactors, where it is subjected to MeV neutron irradiation, low-energy helium isotope particles, and high temperatures. These conditions lead to the formation of point defects, dislocation loops, voids, and transmutation into rhenium (Re) and osmium (Os), which form precipitates that significantly impact dislocation motion and increase hardness. This study uses molecular dynamics modeling to examine the interaction between an edge dislocation and Re-rich particles of various stoichiometries, specifically coherent bcc-phase particles and noncoherent σ -phase precipitates. Results show that shear stress increases by approximately 20–40 % with larger particle size (3–5 nm diameter) and higher Re content (50–75 at.%), while temperature (600–1400 K) has a weak effect on critical shear stress. Coherent bcc-phase particles are weak barriers to dislocations, whereas noncoherent σ -phase precipitates are strong obstacles. The study reveals that dislocations typically cut through these particles, except for noncoherent spherical ones, which are bypassed via the Orowan mechanism.

Keywords: Tungsten, Molecular dynamics method, Dispersion hardening, Deformation, Dislocation

1. Introduction

Tungsten (W) has been selected for the plasma-facing components of the ITER and DEMO fusion reactors due to its highest melting point among metals, good sputtering resistance, high thermal conductivity, and other advantageous properties [1–3]. Its strength and structural integrity are crucial for the long-term and safe operation of the reactor. Therefore, addressing the issue of irradiation embrittlement of W is essential for designing reliable and economically viable components for fusion reactors. W atoms can transmute to rhenium (Re) and subsequently to osmium (Os) when exposed to neutron irradiation [4–8]. According to calculations, initially pure W is expected to contain 3.8 at.% of Re and 1.38 at.% of Os after 5 years of DEMO operation [9]. Even though these

concentrations are well below the solubility limits in W (26 at.% for Re and 5 at.% for Os), neutron irradiation promotes the formation of Re- and Os-containing clusters and precipitates [10,11], which are known to negatively affect the ductility of tungsten [12]. The formation of noncoherent σ - and χ -phase particles has been detected in transmission electron microscopy studies [11–13].

At the same time, W-Re alloys are considered advanced materials for plasma-facing components due to their lower susceptibility to irradiation embrittlement at intermediate temperatures compared to pure W [14–17]. Re plays an important role in inhibiting the migration and/or clustering of vacancies [18,19]. In W-Re alloys, Re suppresses the nucleation of dislocation loops [20]. Increasing the Re content can significantly refine the grain size in W-Re alloys [21]. Since the dissolution energy of

Received 26 August 2024; revised 20 November 2024; accepted 23 November 2024.
Available online 14 December 2024

* Corresponding author.
E-mail address: arseny.m.kazakov@gmail.com (A.M. Kazakov).

<https://doi.org/10.33640/2405-609X.3386>

2405-609X/© 2025 University of Kerbala. This is an open access article under the CC-BY-NC-ND license (<http://creativecommons.org/licenses/by-nc-nd/4.0/>).

deuterium (D) in W-Re alloys is higher than in W, the total amount of D in W decreases significantly when Re is added [22]. Alloying ultra-fine-grained W with Re reduces grain boundary diffusivity [23]. The density of defects after irradiation in pure W is higher than in W-Re alloys [24–26]. Adding Re increases the fracture toughness of W, but only within a limited temperature range of 50–200 °C [27]. W-Re alloy with ZrC or TaC nanoparticles shows high strength with favorable ductility [28–30]. The solid solution softening effect in W depends on temperature and solute concentration [31,32].

However, the advantage of W-Re alloys does not eliminate the need to explore the effect of irradiation-induced precipitation on ductile properties, where both transmuted and pre-existing Re atoms can agglomerate via irradiation-enhanced diffusion. Since preventing the excessive formation of dispersed particles in W or W-Re alloys in a fusion environment is nearly impossible, it is important to understand the consequences of structural evolution and changes in mechanical properties. Additionally, it is crucial to determine the operating conditions under which the detrimental effects of irradiation-induced precipitation are minimized.

Under neutron irradiation, other crystal lattice defects can form in the grains of the material along with precipitates. Collisions of high-energy neutrons with atoms knock them out of their positions, forming a cascade of displaced atoms [33]. After partial relaxation of these cascades, numerous point defects, such as self-interstitial atoms (SIAs) and vacancies, remain and begin to migrate, forming clusters, dislocation loops, or voids [34–38]. As these defects also obstruct dislocation movement, they similarly affect material strength and ductility, albeit to a different extent.

Importantly, excessive precipitation can cause undesirable embrittlement of a material, jeopardizing the reliability of components operating under extreme conditions. A well-known example is the so-called “475 °C embrittlement” in stainless steels, caused by the formation of Cr-rich α' precipitates [39]. In superalloys alloyed with Re, undesired precipitation of close-packed phases can cause embrittlement [40].

The role of irradiation-induced precipitation in the evolution of mechanical properties of materials under irradiation is not fully understood. While some experimental studies have highlighted the impact of rhenium (Re) precipitation on degrading mechanical properties in tungsten (W) alloys [41–43], further research is needed to deepen our understanding. Computer simulations, particularly *ab initio* modeling and molecular dynamics (MD),

provide valuable tools for analyzing microstructural interactions where experiments face limitations.

Ab initio modeling is widely used to estimate point defect energies, dislocation core structures [20, 44–53], mechanical properties, and interactions between solutes and dislocations. It also aids in fitting interatomic potentials for W-W, Re-Re, and W-Re systems. This method has been applied to study Re/Os atom interactions with defects, shedding light on radiation-induced precipitation mechanisms in W [54–56]. However, it requires significant computational resources.

In contrast, MD simulations demand fewer resources and are effective for atomistic-level investigations. They are used to study diffusion along dislocations, interactions between dislocations and defects [57–63], and Re aggregation on dislocation loops in W. MD analyses have examined dislocation-void interactions at various temperatures for W and the interaction between moving dislocations and Re-containing precipitates. These simulations align well with *ab initio* results, offering time-efficient insights into material behavior under irradiation [36, 64–69].

This study utilizes MD simulations to investigate the interaction of edge dislocations with Re-enriched particles in both coherent bcc-phase and noncoherent σ -phase over a temperature range critical for fusion reactor materials. Understanding these interactions is essential for predicting mechanical behavior and enhancing the long-term stability of tungsten-based alloys used in such extreme environments [70–72]. The findings aim to contribute to developing more resilient materials by optimizing alloy composition and microstructural engineering.

This study aims to elucidate the role of temperature and rhenium content in precipitates on the dispersion hardening of tungsten, a critical material for fusion reactors. By analyzing the contribution of different phases with varying shapes, we provide insights into how these phases influence tungsten's mechanical properties post-irradiation. This understanding is crucial for predicting changes in material behavior under reactor conditions, where experimental studies are often challenging.

2. Materials and methods

For this study, the MD method was used, which has proven effective in analyzing various aspects of crystal structure transformation [73], nonlinear lattice dynamics [74], crowdions [75], the thermal stability of nanomaterials [76,77], phase transitions caused by deformation [78], vibrational energy localization

[79,80], deformation mechanisms of high-entropy alloys [81], and many other phenomena.

The simulation was carried out using the Large-scale Atomic/Molecular Massively Parallel Simulator (LAMMPS) [82] and an Embedded Atom Method (EAM) potential for tungsten [83]. The accuracy of different interatomic potentials for W was assessed in the work by Kosarev et al. [84]. The Open Visualization Tool (OVITO) program was used to visualize the simulation results [85].

The computational cell is a single crystal of bcc tungsten, into which the $1/2[111]$ edge dislocation is introduced. The coordinate axes X, Y, Z are oriented along the crystallographic directions [111], $[-1-12]$, and $[1-10]$, respectively. The linear dimensions of the computational cells are $(10\sim 40) \times (15\sim 55) \times 38 \text{ nm}^3$. The cell size is varied along the X and Y axes to account for different defect densities [11–13,25,41,86]. The number of atoms in the cells ranges from 1.3×10^6 to 5.2×10^6 . Strain-controlled shear loading with the strain rate of 10^8 s^{-1} is applied. Stress components other than σ_{xz} are maintained at zero. The lattice parameter of tungsten is $a = 0.316 \text{ nm}$. The length of the Burgers vector of the dislocation is $b = a\sqrt{3}/2 = 0.2736 \text{ nm}$.

To ensure the presence of only one dislocation in the computational cell, fixed boundary conditions are applied along the Z axis, while periodic boundary conditions are imposed in the other two directions. Near the fixed boundaries, atoms are immobile within a 1 nm thick layer. A comparison of results obtained with periodic boundary conditions in all directions versus fixed boundary conditions in one direction and periodic boundary conditions in the other directions was made in the work by Kazakov et al. [65]. The equations of motion for the atoms are integrated using the fourth-order Verlet method with a 2 fs integration step.

The computational cell is shown in Fig. 1. This figure displays (a) a spherical and (b) cylindrical coherent bcc particle in the middle of the cell. To create a spherical or cylindrical coherent bcc particle of a given size, some of the tungsten atoms were replaced with rhenium in the desired ratio (50 or 75 %).

According to experiments, the σ -phase precipitates can occur in various configurations with different stoichiometries depending on temperature and irradiation dose [87,88]. However, irradiation ageing of the material must also be considered. A stable configuration of the σ -phase particle has been determined through modeling [83,89]. In our simulations, spherical or cylindrical σ -phase particles were introduced by replacing the corresponding volume of tungsten crystal with the $L1_0$

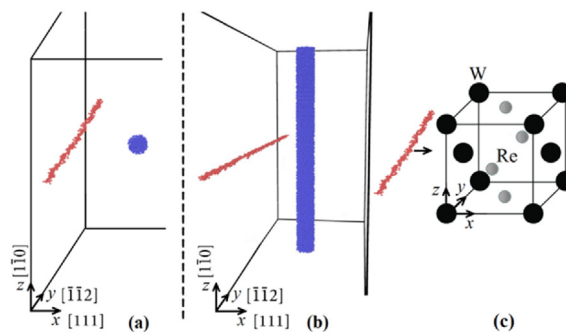


Fig. 1. Visualization of the computational cell. The atoms around the dislocation core are shown in red, the (a) spherical and (b) cylindrical coherent bcc particles are shown in blue. Tungsten atoms are not shown. (c) Crystallographic orientation of the noncoherent σ -phase particle with $L1_0$ superstructure based on the fcc lattice. The dislocation slides in the XY plane along the X axis and the monoatomic planes of W and Re are parallel to the YZ plane. The dislocation moving through the particle creates an antiphase boundary.

superstructure based on the fcc lattice. The phase stoichiometry is WRe. In the $L1_0$ superstructure, monoatomic W and Re planes alternate along one of the planes (100), (010), or (001), creating a tetragonal distortion of the fcc structure. The superstructure has the crystallographic orientation shown in Fig. 1(c). The monoatomic tungsten and rhenium planes are parallel to the YZ plane, so that dislocation sliding along the X axis in the XY plane creates an antiphase boundary in the particle [90]. Note that while the main slip plane in the fcc lattice is (111), in the considered geometry, dislocations are forced to slide in the (100) plane, which is a secondary slip plane.

3. Results and discussion

3.1. Coherent spherical and cylindrical bcc particles

The interaction of the edge dislocation with coherent spherical or cylindrical bcc particles was studied across 16 different sets of modeling parameters, listed in Table 1. Here, C_{Re} represents the content of Re in the particles, L_x and L_y are the corresponding dimensions of the computational cell, and D is the diameter of the particle. The height of cylindrical particles equals 34 nm, which is 4 nm shorter than the size of the computational cell, ensuring that fixed boundary conditions do not affect the particle.

In Fig. 2(a), a typical stress–strain curve for the interaction of the dislocation with a particle (spherical or cylindrical, coherent or noncoherent) is shown. This particular numerical run was conducted with a cylindrical particle of diameter $D = 3 \text{ nm}$, $C_{\text{Re}} = 50 \text{ at.}\%$, $L_x = 20 \text{ nm}$, $L_y = 50 \text{ nm}$, and a

Table 1. Sixteen sets of the simulation parameters for coherent bcc particles.

Set No.	C_{Re} (at.%)	L_x , nm	L_y , nm	D , nm
Spherical bcc-phase particle				
1	50	10	55	3
2	50	20	55	3
3	50	20	55	5
4	50	40	55	5
5	75	10	55	3
6	75	20	55	3
Cylindrical bcc-phase particle				
7	50	10	55	3
8	50	20	55 </td <td>3</td>	3
9	75	10	55	1
10	75	20	55	1
11	75	10	55	2
12	75	20	55	2
13	75	10	55	3
14	75	20	55	3
15	75	20	35	3
16	75	20	15	3

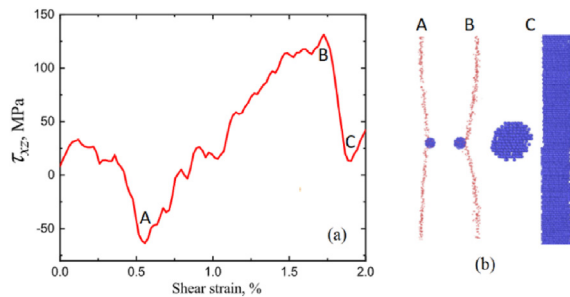


Fig. 2. (a) Example of a typical stress–strain curve for a dislocation interacting with a cylindrical or spherical particle, coherent or noncoherent. (b) The position of the dislocation relative to the particle at different strain values shown in (a): A - the moment of attachment; B - the moment of separation; C - the cut sphere and cylinder particles.

simulation temperature of 800 K. Similar curves were obtained in molecular statics simulations at 0 K [66]. Shear deformation was modeled up to 2 %, which is sufficient for the dislocation to overcome the coherent particle.

In Fig. 2(a), specific strain values are indicated as A, B, and C, with corresponding relative positions of the dislocation and the particle are shown in Fig. 2(b). Negative stress around point A in Fig. 2(a) arises from the attraction between the dislocation and the particle, causing the dislocation to bend towards the particle, as seen in configuration A in Fig. 2(b). It should be noted that the larger the particle size results in a stronger attraction of the dislocation. In the strain range from A to B in Fig. 2(a), linear stress growth is observed, accompanied by bending of the dislocation pinned to the particle. Point B corresponds to the critical shear

stress τ_{xz}^* , at which the dislocation detaches from the particle and the shear stress sharply decreases. Fig. 2(b) shows the spherical and cylindrical particles cut by the passing dislocation. As illustrated, the dislocation shifts half of the coherent bcc particle by the value of one Burgers vector. The maximum bending of the dislocation during cutting the particle is relatively small, as shown in configuration B in Fig. 2(b). This indicates that a defect of this type is a weak obstacle to dislocation, especially in comparison to voids [61].

To assess the effect of temperature on the interaction of a dislocation with a coherent bcc particle, Fig. 3 shows stress–strain relationships obtained at different temperatures. Panels (a) and (b) display the results for spherical and cylindrical particles, respectively. As observed in Fig. 3, an increase in temperature leads to a decrease in the strain at which the dislocation cuts through the particle, with this effect being more pronounced for spherical particle. For spherical particles, the temperature effect is stronger because thermal vibrations of the atoms cause fluctuations in the dislocation line, allowing the dislocation to cut the particle not along the equator plane but with a shift. This shift facilitates cutting since the cross-sectional area of the particle decreases with distance from the equator.

The temperature effect on the magnitude of the critical shear stress is minimal, as shown in Fig. 3. This can be explained as follows: while an increase in temperature enhances the dislocation's ability to cut through the defect, thermal fluctuations also slow down the dislocation's movement due to the Peierls-Nabarro (P-N) barrier. Moreover, the coherent particles are relatively weak obstacles compared to incoherent defects or voids [66]. The effect of temperature on dislocation motion is different at low and high shear stress. At low shear stress the dislocation moves in the P-N relief due to thermal fluctuations and the mobility of the dislocation increases rapidly with temperature. On the other hand, at high shear stress the dislocations

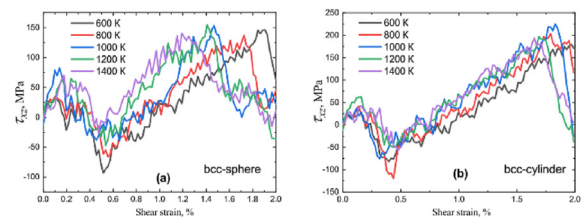


Fig. 3. The stress–strain curves for (a) bcc-sphere and (b) bcc-cylinder particles, for the 1st and 7th sets of simulation parameters from Table 1. In both cases $C_{Re} = 50$ at.%, $L_x = 10$ nm, $L_y = 55$ nm, and $D = 3$ nm. Curves for different simulation temperatures are shown by colors.

slide over the P-N barriers and in this regime increasing temperature increases the viscous friction for the dislocation motion, which slightly reduces its mobility. In our simulations the second regime is realized, when the effect of temperature on dislocation motion is weak. This trend is consistent across all parameter sets presented in Table 1.

The next step is to analyze the effect of computational cell size, which influences the density of defects in the crystal. This variation is examined to study different defect densities according to experimental data [11–13,25,41,86]. For this analysis, a cylindrical coherent particle with a diameter of $D = 3$ nm and containing $C_{Re} = 75$ at.% rhenium is used. The study varies the cell sizes L_x and L_y , focusing on parameter sets 13 through 16 from Table 1.

The results are presented in Fig. 4. Comparing panels (a) and (b) shows the effect of increasing L_x from 10 nm to 20 nm while keeping $L_y = 55$ nm constant. It can be observed that doubling L_x results in an increase of τ_{xz}^* by 10–20 % across different temperatures. This relatively weak dependence of the maximum shear stress on L_x is attributed to the interaction between the considered dislocation and other dislocations in the system, a consequence of using periodic boundary conditions.

Additionally, in panels (b), (c), and (d), with $L_x = 20$ nm and varying L_y to 55, 35, and 15 nm, the maximum shear stress τ_{xz}^* increases rapidly as L_y decreases, i.e., as the length of the dislocation segment between obstacles increases. This effect is explained by the Bacon-Kocks-Scattergood (BKS) theory [91], which is discussed in detail below.

Table 2 presents the values of the critical shear stress for all simulation parameter sets listed in Table 1 and for all temperatures. From the analysis of these data the following observations can be made.

An increase in the rhenium content in the coherent spherical particles from 50 % to 75 % results in a 20–40 % increase in obstacle strength, as seen when comparing sets 1 and 2 with sets 5 and 6. For cylindrical particles, the increase in obstacle strength is smaller, around 10 %, as evidenced by comparing sets 7 and 8 with sets 13 and 14. In some cases, a lower rhenium content yielded higher τ_{xz}^* but this variation falls within the data scatter caused by thermal oscillations.

Increasing the diameter of the spherical particle from 3 nm to 5 nm results in an average increase of τ_{xz}^* by 20 %, as observed when comparing sets 1 and 2 with sets 3 and 4 in Table 2. For cylindrical defects, parameter sets 9 and 10 correspond to $D = 1$ nm, sets 11 and 12 to $D = 2$ nm, and sets 13 and 14 to

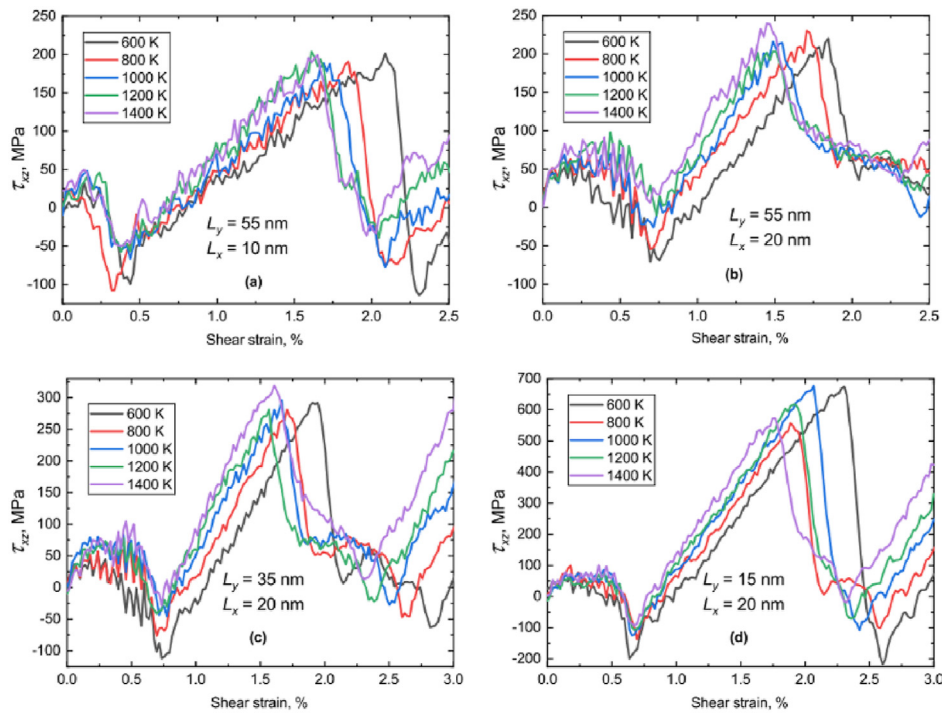


Fig. 4. (a–d) Stress–strain curves for the interaction of the dislocation with the bcc-cylinder particle for parameter sets 13 to 16, respectively (see Table 1). The cylinder diameter is 3 nm and $C_{Re} = 75$ at.%. The values of L_x and L_y are given in the panels. The colors of the curves corresponding to the simulation temperatures of 600, 800, 1000, 1200, and 1400 K are shown in the legends.

Table 2. The critical shear stress for coherent bcc particles for different temperatures. The last column gives the averaged values.

Set No.	τ_{xz}^* , MPa					τ_{xz}^{*aver} , MPa
	600 K	800 K	1000 K	1200 K	1400 K	
Spherical bcc-phase particle						
1	146.7	137.4	153.6	155.0	140.1	147
2	152.8	149.6	156.2	146.8	143.7	150
3	183.6	188.8	179.8	190.5	187.6	186
4	192.4	191.9	185.2	178.6	192.3	188
5	195.1	194.7	201.4	199.1	200.8	198
6	197.3	200.6	191.3	194.9	203.7	198
Cylindrical bcc-phase particle						
7	179.8	203.5	225.7	197.0	194.2	200
8	187.5	201.8	200.2	192.3	186.4	194
9	71.2	77.8	72.4	80.0	78.5	75.6
10	91.7	93.6	87.9	88.0	90.2	90.3
11	139.4	137.8	137.3	143.8	136.6	139
12	158.5	148.1	135.5	135.6	139.7	143
13	201.3	190.9	188.1	203.9	199.3	197
14	220.2	227.3	216.0	203.1	240.1	221
15	291.9	280.9	295.7	281.4	318.9	294
16	674.5	556.6	677.1	616.6	573.3	620

$D = 3$ nm. As shown in Table 2, the obstacle strength increases approximately linearly with the diameter of the cylindrical particle.

It appears that in most cases, 1.2 times higher shear stress is required to cut the cylindrical particle compared to the spherical one. This difference can be attributed to the ability to cut the spherical particle with a shift away from the equatorial plane, facilitated by dislocation line fluctuations caused by thermal vibrations of atoms.

3.2. Noncoherent σ -phase particles

Now, let us consider the interaction between edge dislocations and noncoherent σ -phase particles. Eight sets of simulation parameters were studied and analyzed, as detailed in Table 3.

A key difference between coherent and noncoherent particles is that the latter introduce misfit dislocations in the tungsten matrix, which will be

Table 3. Simulation parameters for noncoherent σ -phase particle.

Set No.	C_{Re} (at. %)	L_x , nm	L_y , nm	D , nm
Spherical σ -phase particle				
1	50	10	55	3
2	50	20	55	3
3	50	20	55	5
4	50	40	55	5
Cylindrical σ -phase particle				
5	50	10	55	3
6	50	20	55	3
7	50	20	35	3
8	50	20	15	3

discussed in more detail later. Crystal lattice defects around precipitates have also been observed experimentally [11,12]. Before the edge dislocation interacts with the particle, it first encounters the misfit dislocations. Since σ -phase particles require higher stress and strain to be cut compared to coherent bcc particles, a shear strain of up to 3.5 % was applied for spherical particles and up to 4 % for cylindrical particles.

The effect of the computational cell size is examined by analyzing the results shown in Fig. 5. In this analysis, the dislocation interacts with a cylindrical noncoherent particle of diameter $D = 3$ nm at different temperatures ranging from 600 to 1400 K. In panels (a) and (b), $L_y = 55$ nm, with L_x set to 10 and 20 nm, respectively. An increase in L_x by a factor of two results in a corresponding increase in the maximum shear stress τ_{xz}^* by a factor of two, a much stronger effect compared to the coherent particle, as shown in Fig. 4(a and b). This pronounced influence of L_x for noncoherent particles is due to the increase in the number of misfit dislocations around the particle as L_x increases from 10 to 20 nm.

The results for different values of L_y with $L_x = 20$ nm are shown in Fig. 5(b-d). For L_y values of 55, 35, and 15 nm, the maximum shear stress increases and reaches approximately 1050, 1300, and 1900 MPa, respectively. Here, L_y represents the length of the dislocation segment between two obstacles. The observed increase in τ_{xz}^* with decreasing L_y is explained by the BKS theory [91] and the interaction between the edge dislocation and the misfit dislocations, which will be discussed in more detail later.

The comparison of stress–strain curves for spherical and cylindrical σ -phase particles is shown in Fig. 6(a and b). The parameters are $L_x = 20$ nm, $L_y = 55$ nm, and $D = 3$ nm (corresponding to the 3rd and 6th sets of simulation parameters from Table 3). Results for temperatures ranging from 600 to 1400 K in 200 K increments are compared. As illustrated in Fig. 6, the curves exhibit a similar shape to those for coherent bcc particles, with some distinctions. The initial peak occurs when the dislocation interacts with the particle. The increase in shear stress as the dislocation approaches the particle is attributed to the interaction with misfit dislocations, which is not present with coherent bcc particles. The subsequent linear increase indicates that the dislocation is overcoming the obstacle, and at the maximum shear stress τ_{xz}^* the dislocation has passed through the particle.

The obstacle strength for σ -phase particles, calculated for all sets of model parameters listed in Table 3, is summarized in Table 4. The dependence

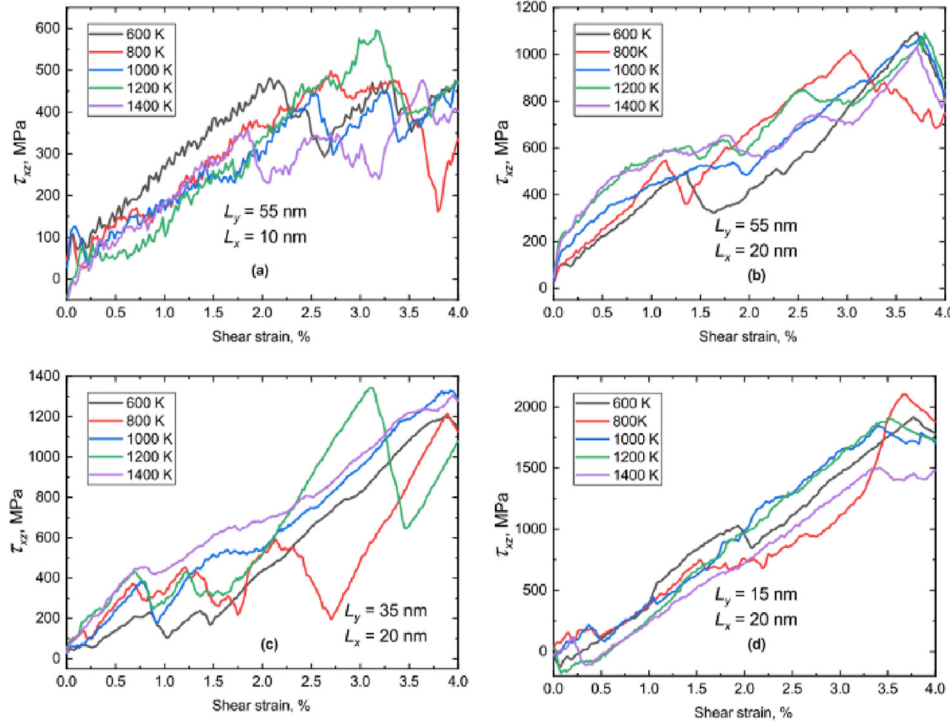


Fig. 5. Stress strain curves for the interaction of dislocation with noncoherent σ -phase cylinder particle of diameter $D = 3$ nm. Values of L_x and L_y are indicated in each panel. The colors of the curves corresponding to the simulation temperatures of 600, 800, 1000, 1200, and 1400 K are shown in the legends.

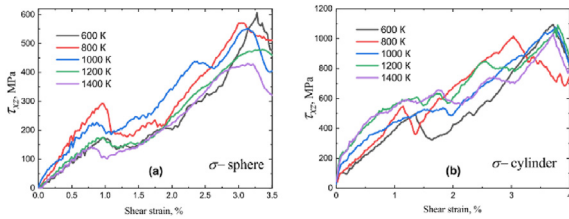


Fig. 6. The stress–strain curves for (a) the spherical σ -phase particle, 2nd set of parameters from Table 3, and (b) σ -phase cylinder precipitate, 6th set from Table 3. In both cases $L_x = 20$ nm, $L_y = 55$ nm, and $D = 3$ nm. The colors of the curves corresponding to the simulation temperatures of 600, 800, 1000, 1200, and 1400 K are shown in the legends.

of τ_{xz}^* on model parameters for noncoherent particles is similar to that for coherent bcc-phase particles. Increasing the precipitate diameter D and the parameter L_y both lead to an increase in τ_{xz}^* . High temperatures generally make it easier for the dislocation to overcome the obstacle, though the effect of temperature is not pronounced. Notably, cylindrical σ -phase particles are approximately twice as strong as spherical ones due to differences in interaction mechanisms. In contrast to the bcc particles, where the dislocation slips in the primary slip system, the noncoherent σ -phase particles force dislocation slip in the secondary slip system.

Table 4. The critical shear stress for noncoherent σ -phase particles for different temperatures. The last column gives the averaged values.

Set No.	τ_{xz}^* , MPa					τ_{xz}^* , MPa
	600 K	800 K	1000 K	1200 K	1400 K	
Spherical σ -phase particle						
1	520.1	544.7	533.9	515.2	567.6	537
2	606.6	570.7	551.1	478.9	430.2	528
3	761.2	805.8	785.3	767.8	789.8	781
4	877.6	856.9	871.0	895.3	834.7	867
Cylindrical σ -phase particle						
5	470.6	498	465.8	595.9	476.3	490
6	1094	1017	1076	1090	1030	1061
7	1203	1215	1330	1344	1305	1297
8	1918	2106	1845	1903	1502	1855

Additionally, the noncoherent particles generate misfit dislocations, which enhance the overall obstacle strength. The dislocation also expends energy creating antiphase boundaries within the noncoherent particle.

3.3. Details of the interaction of the dislocation with the noncoherent particles and surrounding misfit dislocations

There are two primary mechanisms for dislocation-precipitate interaction: the formation of the

Orowan ring [92–95] and the cutting of the precipitate [96–98]. In our simulations, the edge dislocation cut through spherical and cylindrical coherent particles, as well as cylindrical noncoherent particles, while the spherical noncoherent particles were bypassed using the Orowan mechanism. Cutting bcc coherent particles is relatively straightforward because the dislocation moves in the primary slip plane, which is (100). For σ -phase particles with an fcc lattice, the main slip plane is (111). However, in our simulations, the maximum Schmidt factor is achieved in the secondary slip plane (100). This results in dislocation movement in both slip planes – (100) and (111) – within the cylindrical σ -phase particles.

The interaction between the edge dislocation and the cylindrical noncoherent particle, along with the misfit dislocations surrounding the particle, is illustrated in Fig. 7. Common Neighbor Analysis (CNA) [99] is used to visualize the atoms around the dislocations and other defects, while the dislocation analysis function [100] highlights dislocations across different slip systems. The significant number of defects around the precipitate contributes to the increased obstacle strength, as edge dislocations interact with these misfit dislocations. Additionally, the $L1_0$ ordered structure of the precipitate is a factor in hardening, as dislocations sliding through the structure create antiphase boundaries, consuming extra energy in the process.

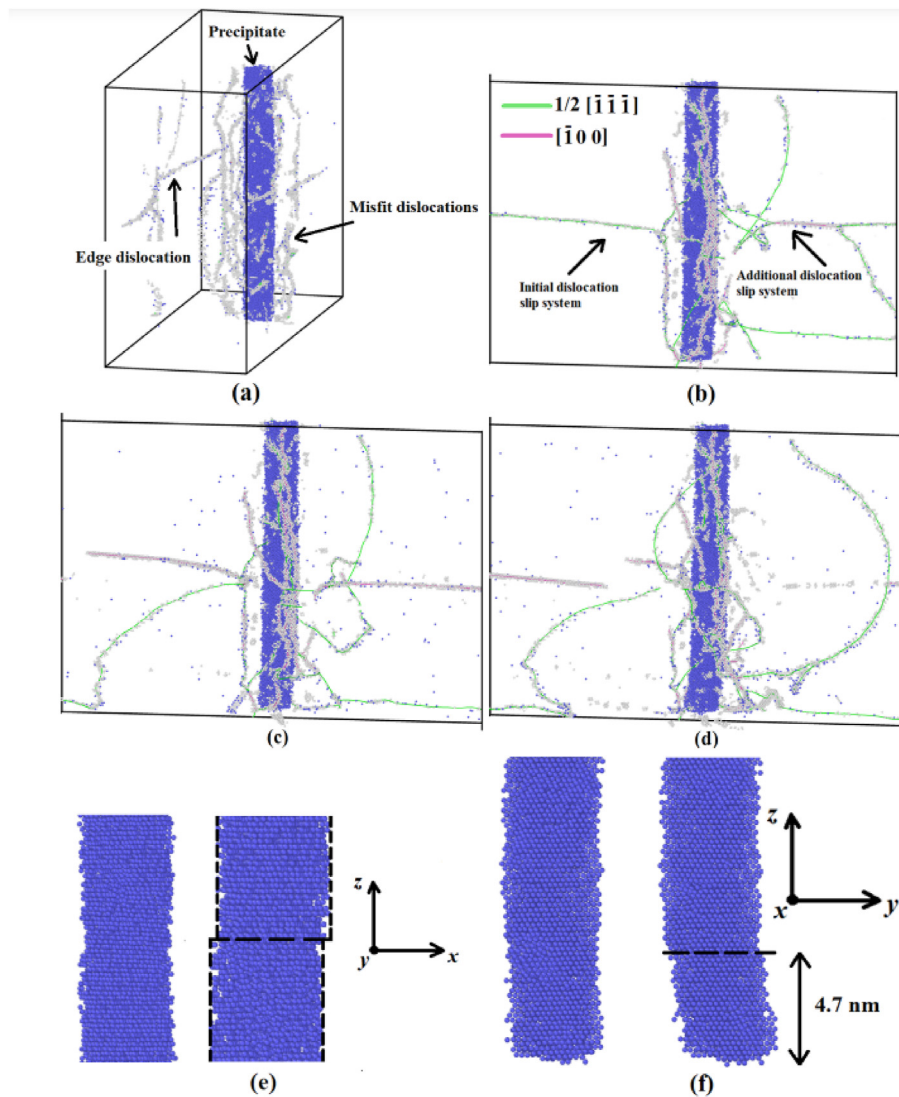


Fig. 7. (a) Initial position of an edge dislocation and σ -cylinder precipitate; (b), (c), (d) dislocation behavior during deformation at 1.6 %, 2.5 %, and 3.5 % shear strain, respectively. Dislocations marked with green and pink lines belong to different dislocation slip systems. (e) σ -cylinder precipitate profile (middle part) after cutting, projected on the XZ plane; (f) σ cylinder precipitate profile (bottom part) after cutting, projected on the YZ plane. The simulation temperature is 600 K, $L_x = 20$ nm, $L_y = 55$ nm, and $D = 3$ nm. Cylindrical σ -precipitate is shown in blue, atoms of the disordered structure are shown in gray, they surround the dislocation cores and other defects.

For the interaction of an edge dislocation with a spherical σ -phase particle, the Orowan bypass mechanism is observed, as shown in Fig. 8. The atoms in the simulation cell are color-coded using the CNA method to illustrate this process. This strengthening mechanism is commonly studied in bcc metals [95], but has not been observed in molecular statics simulations [66]. The smaller number of misfit dislocations around the spherical σ -phase particle compared to cylindrical particles results in a higher energy requirement for cutting the precipitate and forming antiphase boundaries. Instead, the Orowan ring formation is more favorable. In contrast, the cylindrical precipitates, with their greater number of misfit dislocations, compel the edge dislocation to cut through the particle rather than bypassing it, thus preventing the realization of the Orowan mechanism.

To evaluate the dependence of dislocation density on shear strain, Fig. 9 presents the results for spherical and cylindrical σ -phase particles. Panels (a) and (b) compare the dislocation densities for these two types of particles.

The dislocation density was calculated using the dislocation analysis function in OVITO, with measurements taken every 0.5 % of shear strain.

As shown in Fig. 9, the dislocation density as a function of shear strain varies between spherical and cylindrical σ -phase particles. For spherical particles, the dislocation density increases almost linearly with strain and tends to rise with temperature. This increase is primarily due to the formation of Orowan rings around the particles. The observed increase in dislocation density with temperature for spherical σ -precipitates, as shown in Fig. 9, can be attributed to enhanced dislocation mobility that which may be the result of increased diffusion and mass transfer often observed when a material is exposed to extreme conditions [102–105] and the formation of Orowan loops. At elevated temperatures, dislocations gain additional thermal energy, facilitating their movement and allowing for more frequent interactions with the precipitates. This interaction enables dislocations to bypass the precipitates by forming Orowan loops, which is energetically favorable at higher temperatures. Furthermore, increased thermal

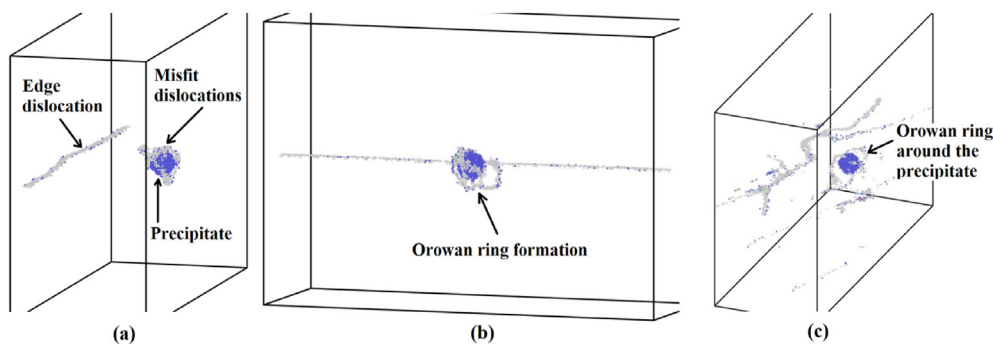


Fig. 8. (a) Starting position of an edge dislocation and σ -sphere precipitate surrounded by the misfit dislocations; (b) Orowan ring formation during deformation; (c) Orowan ring around the σ -precipitate after dislocation unpinning. The simulation temperature is 600 K, $L_y = 20$ nm, and $D = 3$ nm. The spherical σ -precipitate is shown in blue, the atoms of the disordered structure are shown in gray.

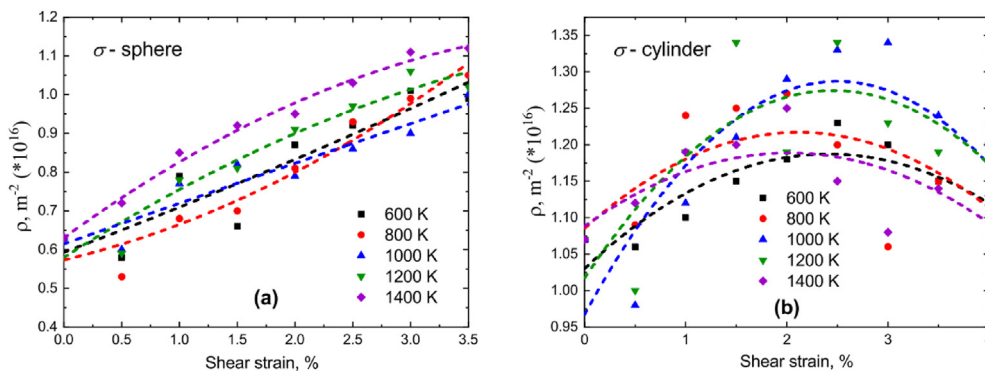


Fig. 9. Dependence of dislocation density on shear strain for (a) spherical and (b) cylindrical σ -phase particles. The simulation results for different temperatures are shown in different colors according to the legend. The short dashed lines show the polynomial fit.

energy may promote the generation of new dislocations through mechanisms such as dynamic recovery. As a result, the overall average dislocation density increases with temperature, exhibiting a nearly linear dependence.

In contrast, the dislocation density for cylindrical particles exhibits nonmonotonic behavior: It initially increases with strain but then decreases. This complex behavior is attributed to the interaction of the edge dislocation with misfit dislocations and the dislocation's movement across two slip systems, as illustrated in Fig. 7(b), where dislocations are seen sliding in the (-100) and (-1-1-1) planes.

3.4. Application of the BKS model

The effect of temperature on the dislocation-precipitate interaction was found to be relatively modest. Therefore, the maximum shear stress can be described using the BKS analytical model, which does not account for temperature effects but incorporates the interaction between dislocation lines that bow between obstacles [91]. This model considers the formation of a pair of screw dislocations with opposite Burgers vectors, which significantly influences the mechanical properties of the material. Although the BKS theory is designed for interactions with impenetrable obstacles, we compare its theoretical predictions with numerical results for cylindrical coherent and noncoherent particles, which are overcome through cutting.

According to the BKS theory, the critical shear stress for an impenetrable obstacle is [91]:

$$\tau_{BKS}^{max} = \frac{\mu b}{2\pi L'} \left[\ln \left(\frac{1}{D^{-1} + L'^{-1}} \right) + 0.7 \right], \quad (1)$$

where $\mu = 160$ GPa is the shear modulus of the tungsten matrix, $b = 0.2736$ nm is the length of the Burgers vector, $L' = L_y - D$ is the length of the straight dislocation segment between precipitates.

According to the BKS theory, when the dislocation length L_y decreases, the stress required to overcome the precipitate increases. If the diameter of precipitate D increases, then τ_{xz}^{max} also increases.

The analytical estimate of τ_{xz}^{max} is presented in Table 5 for different values of L_y and precipitate diameter $D = 3$ nm. Three values of τ_{xz}^{max} presented in Table 5 are compared with the numerical values $\tau_{xz}^{*,aver}$ for the cylindrical bcc coherent particle (Table 2, parameter sets 6, 7, and 8) and cylindrical σ -phase noncoherent particles (Table 4, parameter sets 6, 7, and 8). It can be seen that for the coherent particles $\tau_{xz}^{*,aver} < \tau_{BKS}^{max}$, because in this case the particles

Table 5. τ_{BKS}^{max} according to Eq. (1) for different L_y values and particle of diameter $D = 3$ nm; numerically found $\tau_{xz}^{*,aver}$ for the coherent and noncoherent cylindrical precipitates; effective diameter of the cylindrical precipitate surrounded by misfit dislocations.

L_y , nm	τ_{BKS}^{max} , MPa	$\tau_{xz}^{*,aver}$, MPa coherent	$\tau_{xz}^{*,aver}$, MPa noncoherent	D_{eff} , nm
55	234	221	1061	33.5
35	372	294	1297	19.6
15	915	620	1855	7.4

are not overcome by the Orowan mechanism, rather being cut with a less shear stress. Thus, for the bcc coherent particles, the numerical results obtained are in agreement with the BKS theory. On the other hand, for the coherent particles one has $\tau_{xz}^{*,aver} > \tau_{BKS}^{max}$, although they are also overcome by cutting. The explanation is the presence of misfit dislocations around the noncoherent particles. Such defects increase the strength of the obstacle by effectively increasing its diameter. The last column of Table 5 gives the effective diameters D_{eff} obtained from the conditions that Eq. (1) gives the maximum shear stress equal to $\tau_{xz}^{*,aver}$ for the noncoherent particle. It can be seen that D_{eff} increases with increasing L_y and this correlates with the fact that the number of misfit dislocations increases with increasing L_y .

4. Conclusions

In general, one can conclude that our findings provide a detailed understanding of how temperature and rhenium content in precipitates affect tungsten's mechanical properties. The results align with previous studies that highlight the role of Re in enhancing ductility and reducing defect clustering in W-Re alloys [14–17]. The observed increase in shear stress with larger particle size and higher Re content corroborates existing literature on precipitation hardening mechanisms. Furthermore, our study extends current knowledge by demonstrating the distinct behaviors of coherent and noncoherent particles under irradiation, which is consistent with the known effects of misfit dislocations on material strength [41–43]. By situating our results within this broader context, we offer insights into optimizing tungsten alloys for improved performance in fusion reactors. This work suggests potential pathways for future research, such as exploring chi-phase and hcp-phase particle interactions, to further enhance our understanding of dispersion hardening in irradiated tungsten.

Our study includes coherent bcc particles with 50 or 75 at.% rhenium and noncoherent σ -phase precipitates of WRe composition, characterized by an

$L1_0$ ordered structure based on an fcc lattice. The particles are modeled as either spherical or cylindrical. The effects of temperature, particle size, and computational cell size on the dislocation-particle interaction are analyzed.

It is found that the coherent bcc particles (both spherical and cylindrical) are weak obstacles, in agreement with the previous study [101], and both are cut after interaction with the edge dislocation. The obstacle strength of coherent precipitates depends on the simulation parameters as follows: the critical shear stress τ_{xz}^* increases almost linearly with the defect diameter for the cylindrical precipitates. The rhenium content influences the hardening even more than the defect size - an increase of C_{Re} from 50 to 75 at.% leads to an increase of the obstacle strength by 20–40 % for spherical and by 10 % for cylindrical precipitates. The shape of the precipitate also has an effect on hardening: approximately 1.2 times higher shear stress is required to cut the cylindrical particle compared to the spherical one. This can be explained by the fact that the particle is not cut by the dislocation through the equatorial plane, but with a shift due to the fluctuation of the dislocation line caused by the thermal vibrations of the atoms.

Noncoherent σ -phase particles are much stronger obstacles than coherent bcc particles. Firstly, the misfit dislocations surround the noncoherent particles and these dislocations are different for cylindrical and spherical particles. Therefore, the edge dislocation interacts differently with spherical and cylindrical noncoherent particles. The spherical σ -phase particles of 3 or 5 nm diameter are overcome by the Orowan mechanism and dislocation loops (Orowan rings) are formed around the precipitate, which is probably due to the complex interaction of the edge dislocation with the misfit dislocations. On the other hand, cylindrical σ -phase precipitates are cut by the edge dislocation similar to cylindrical coherent bcc particles, but it requires much higher shear stress due to the following reasons:

- Before the edge dislocation reaches the cylindrical precipitate, it interacts with misfit dislocations, which increases the obstacle strength;
- The main slip plane in the fcc σ -phase particles is (111), but the maximum Schmidt factor in the considered simulation setup is realized for the secondary slip plane (100). This is the reason for the observed dislocation sliding in the cylindrical σ -phase particle in two slip planes, (100) and (111), and the precipitate is cut in two planes, see Fig. 8;

- When a dislocation cuts the ordered σ -phase, an antiphase boundary is created, which inhibits the dislocation sliding.

The effect of temperature on the magnitude of the critical shear stress, τ_{xz}^* , is not significant (see Tables 2 and 4). This is because two opposing factors are at play. As temperature increases, the strain required for the dislocation to cut through the particle decreases due to enhanced atomic vibrations. However, at higher temperatures, the sliding of the dislocation is slowed down because it encounters a higher P-N barrier. This interplay between the reduction in required strain and the increased difficulty of dislocation motion at higher temperatures results in only a modest effect on the critical shear stress.

As the cell size L_x increases, the dislocation density decreases, and the maximum shear stress τ_{xz}^* slightly increases. Conversely, reducing L_y , which represents the distance between precipitates, leads to a rapid increase in the critical shear stress, consistent with the predictions of the BKS theory [91].

The BKS theory accurately predicts that bcc coherent particles should be cut by the edge dislocation, as the calculated Orowan stress exceeds the critical stress observed in simulations where the particles were indeed cut (see Table 5). However, for noncoherent particles, the BKS theory cannot predict the obstacle strength because it does not account for crucial hardening factors such as the presence of misfit dislocations.

Overall, the results are consistent with the molecular statics study [66] and offer valuable insights for enhancing the properties of reactor materials. Future research will focus on the interaction of dislocations with χ -phase and hcp-phase particles in tungsten to achieve a comprehensive understanding of the mechanisms behind dispersion hardening in tungsten.

Funding

The research was carried out with the support of the Ministry of Science and Higher Education of the Russian Federation within the framework of the State assignment “Study of physical and mechanical processes in the formation and strengthening of parts for aerospace and transport equipment” No. FEUE-2023-0006.

Ethics information

This study did not involve human participants or animals, and ethical approval was not required according to the institutional and national guidelines.

References

- [1] J. Knaster, A. Moeslang, T. Muroga, Materials research for fusion, *Nat. Phys.* 12 (2016) 424–434, <https://doi.org/10.1038/nphys3735>.
- [2] A.R. Raffray, R. Nygren, D.G. Whyte, S. Abdel-Khalik, R. Doerner, F. Escourbiac, T. Evans, R.J. Goldston, D.T. Hoelzer, S. Konishi, P. Lorenzetto, M. Merola, R. Neu, P. Norajitra, R.A. Pitts, M. Rieth, M. Roedig, T. Rognlien, S. Suzuki, M.S. Tillack, C. Wong, High heat flux components—readiness to proceed from near term fusion systems to power plants, *Fusion Eng. Des.* 85 (2010) 93–108, <https://doi.org/10.1016/j.fusengdes.2009.08.002>.
- [3] H. Bolt, V. Barabash, G. Federici, J. Linke, A. Loarte, J. Roth, K. Sato, Plasma facing and high heat flux materials – needs for iter and beyond, *J. Nucl. Mater.* 307–311 (2002) 43–52, [https://doi.org/10.1016/S0022-3115\(02\)01175-3](https://doi.org/10.1016/S0022-3115(02)01175-3).
- [4] X. Hu, C.M. Parish, K. Wang, T. Koyanagi, B.P. Eftink, Y. Katoh, Transmutation-induced precipitation in tungsten irradiated with a mixed energy neutron spectrum, *Acta Mater.* 165 (2019) 51–61, <https://doi.org/10.1016/j.actamat.2018.11.032>.
- [5] M. Klimenkov, M. Durrschnabel, U. Jantsch, P. Lied, M. Rieth, H.C. Schneider, D. Terentyev, W. Van Renterghem, Microstructural analysis of W irradiated at different temperatures, *J. Nucl. Mater.* 572 (2022) 154018, <https://doi.org/10.1016/j.jnucmat.2022.154018>.
- [6] M.J. Lloyd, A.J. London, J.C. Haley, M.R. Gilbert, C.S. Becquart, C. Domain, E. Martinez, M.P. Moody, P.A.J. Bagot, D. Nguyen-Manh, D.E.J. Armstrong, Interaction of transmutation products with precipitates, dislocations and grain boundaries in neutron irradiated W, *Materialia* 22 (2022) 101370, <https://doi.org/10.1016/j.mtla.2022.101370>.
- [7] R.G. Abernethy, J.S.K.-L. Gibson, A. Giannattasio, J.D. Murphy, O. Wouters, S. Bradnam, L.W. Packer, M.R. Gilbert, M. Klimenkov, M. Rieth, H.-C. Schneider, C.D. Hardie, S.G. Roberts, D.E.J. Armstrong, Effects of neutron irradiation on the brittle to ductile transition in single crystal tungsten, *J. Nucl. Mater.* 527 (2019) 151799, <https://doi.org/10.1016/j.jnucmat.2019.151799>.
- [8] T. Koyanagi, N.K. Kumar, T. Hwang, L.M. Garrison, X. Hu, L.L. Snead, Y. Katoh, Microstructural evolution of pure tungsten neutron irradiated with a mixed energy spectrum, *J. Nucl. Mater.* 490 (2017) 66–74, <https://doi.org/10.1016/j.jnucmat.2017.04.010>.
- [9] M.R. Gilbert, J.-C. Sublet, Neutron-induced transmutation effects in W and W-alloys in a fusion environment, *Nucl. Fusion* 51 (2011) 043005, <https://doi.org/10.1088/0029-5515/51/4/043005>.
- [10] R.K. Williams, F.W. Wiffen, J. Bentley, J.O. Stiegler, Irradiation induced precipitation in tungsten based, W-Re alloys, *Metal. Trans. A.* 14 (1983) 655–666, <https://doi.org/10.1007/bf02643781>.
- [11] M. Fukuda, K. Yabuuchi, S. Nogami, A. Hasegawa, T. Tanaka, Microstructural development of tungsten and tungsten–rhenium alloys due to neutron irradiation in HFIR, *J. Nucl. Mater.* 455 (2014) 460–463, <https://doi.org/10.1016/j.jnucmat.2014.08.002>.
- [12] Y. Nemoto, A. Hasegawa, M. Satou, K. Abe, Microstructural development of neutron irradiated W-Re alloys, *J. Nucl. Mater.* 283 (2000) 1144–1147, [https://doi.org/10.1016/S0022-3115\(00\)00290-7](https://doi.org/10.1016/S0022-3115(00)00290-7).
- [13] T. Tanno, A. Hasegawa, M. Fujiwara, J.-C. He, S. Nogami, M. Satou, T. Shishido, K. Abe, Precipitation of solid transmutation elements in irradiated tungsten alloys, *Mater. Trans.* 49 (2008) 2259–2264, <https://doi.org/10.2320/matertrans.MAW200821>.
- [14] S. Watanabe, S. Nogami, J. Reiser, M. Rieth, S. Sickinger, S. Baumgartner, T. Miyazawa, A. Hasegawa, Tensile and impact properties of tungsten–rhenium alloy for plasma-facing components in fusion reactor, *Fusion Eng. Des.* 148 (2019) 111323, <https://doi.org/10.1016/j.fusengdes.2019.111323>.
- [15] S. Nogami, D. Terentyev, A. Zinovev, C. Yin, M. Rieth, G. Pintsuk, A. Hasegawa, Neutron irradiation tolerance of potassium-doped and rhenium-alloyed tungsten, *J. Nucl. Mater.* 553 (2021) 153009, <https://doi.org/10.1016/j.jnucmat.2021.153009>.
- [16] D.D. Caillard, A TEM in situ study of the softening of tungsten by rhenium, *Acta Mater* 194 (2020) 249–256, <https://doi.org/10.1016/j.actamat.2020.04.039>.
- [17] T. Karafi, A. Tahiri, M. Idiri, C. Chabba, B. Boubeker, Effect the concentration of rhenium on the mechanical properties and dislocation mechanisms of tungsten–rhenium alloy, *Int. J. Tech. Phys. Probl. Eng.* 15 (2023) 220–225.
- [18] D.E.J. Armstrong, T.B. Britton, Effect of dislocation density on improved radiation hardening resistance of nano-structured tungsten–rhenium, *Mater. Sci. Eng. A.* 611 (2014) 388–393, <https://doi.org/10.1016/j.msea.2014.06.013>.
- [19] Z. Wang, L. Gao, X.-L. Zhu, Y. Yuan, S. Wang, L. Cheng, G.-H. Lu, Effect of rhenium on defects evolution behavior in tungsten under irradiation, *Nucl. Fusion* 61 (2021) 036037, <https://doi.org/10.1088/1741-4326/abd920>.
- [20] T. Xin, Y. Yang, Y. Wang, L. Wu, R. Pan, Q. Xu, X. Wu, Evolution of irradiation defects in W and W-Re systems: a density functional theory and rate theory study, *Metals* 13 (12) (2023) 1990, <https://doi.org/10.3390/met13121990>.
- [21] F. Luo, H. Luo, Q. Liu, L. Zhou, W. Lin, Z. Xie, L. Guo, The effect of rhenium content on microstructural changes and irradiated hardening in W-Re alloy under high-dose ion irradiation, *Nanomaterials* 13 (2023) 497, <https://doi.org/10.3390/nano13030497>.
- [22] B.-Y. Wu, Y.-P. Xu, Y.-M. Lyu, X.-C. Li, X. Geng, S.-A. Puyang, X. Shen, X.-D. Pan, H.-S. Zhou, G.-N. Luo, Effects of rhenium content on the deuterium permeation and retention behavior in tungsten, *J. Nucl. Mater.* 565 (2022) 153709, <https://doi.org/10.1016/j.jnucmat.2022.153709>.
- [23] J. Kappacher, O. Renk, D. Kiener, H. Clemens, V. Maier-Kiener, Controlling the high temperature deformation behavior and thermal stability of ultra-fine-grained W by Re alloying, *J. Mater. Res.* 36 (2021) 2408–2419, <https://doi.org/10.1557/s43578-020-00026-z>.
- [24] J. He, G.Y. Tang, A. Hasegawa, K. Abe, Microstructural development and irradiation hardening of W and W-(3–26) wt%Re alloys after high-temperature neutron irradiation to 0.15 dpa, *Nucl. Fusion* 46 (2006) 877–883, <https://doi.org/10.1088/0029-5515/46/11/001>.
- [25] M. Fukuda, T. Tanno, S. Nogami, A. Hasegawa, Effects of Re content and fabrication process on microstructural changes and hardening in neutron irradiated tungsten, *Mater. Trans.* 53 (2012) 2145–2150, <https://doi.org/10.2320/matertrans.MBW201110>.
- [26] T. Hwang, M. Fukuda, S. Nogami, A. Hasegawa, H. Usami, K. Yabuuchi, K. Ozawa, H. Tanigawa, Effect of self-ion irradiation on hardening and microstructure of tungsten, *Nucl. Mater. Energy.* 9 (2016) 430–435, <https://doi.org/10.1016/j.nme.2016.06.005>.
- [27] Y.-H. Zhang, E. Ma, J. Sun, W.-Z. Han, Unveiling the intrinsic rhenium effect in tungsten, *Acta Mater* 264 (2024) 119586, <https://doi.org/10.1016/j.actamat.2023.119586>.
- [28] S. Miao, Y. Zhao, Z. Xie, L. Zeng, Y. Lin, On the ductilization and the resistance to annealing-induced embrittlement of high-strength W-Re and nano-particle doped W-Re-ZrC alloys, *Mater. Sci. Eng. A.* 861 (2022) 144334, <https://doi.org/10.1016/j.msea.2022.144334>.
- [29] R. Liu, W. Zhao, Y. Tian, J. Zhang, G. Luo, Q. Shen, The synergetic effect of TaC particles and Re alloy on microstructure and mechanical properties in tungsten alloy, *J. Mater. Res. Tech.* 28 (2024) 4639–4646, <https://doi.org/10.1016/j.jmrt.2024.01.035>.
- [30] Z. Zheng, C. Lai, W. Zhou, Y. Wang, Y. Zhang, J. Wang, Preparation, mechanical properties and strengthening mechanism of W-Re alloys: a review, *Materials* 17 (2024) 102, <https://doi.org/10.3390/ma17010102>.

- [31] Y. Zhao, J. Marian, Direct prediction of the solute softening-to-hardening transition in W-Re alloys using stochastic simulations of screw dislocation motion, *Model. Simul. Mater. Sci. Eng.* 26 (2018) 045002, <https://doi.org/10.1088/1361-651X/aaeacf>.
- [32] J. Kappacher, A. Leitner, D. Kiener, H. Clemens, V. Maier-Kiener, Thermally activated deformation mechanisms and solid solution softening in W-Re alloys investigated via high temperature nanoindentation, *Mater. Des.* 189 (2020) 108499, <https://doi.org/10.1016/j.matdes.2020.108499>.
- [33] J. Byggmatar, F. Granberg, A.E. Sand, A. Pirttikoski, R. Alexander, M.-C. Marinica, K. Nordlund, Collision cascades overlapping with self-interstitial defect clusters in Fe and W, *J. Phys. Condens. Matter.* 21 (2019) 245402, <https://doi.org/10.1088/1361-648X/ab0682>.
- [34] B.N. Singh, S.I. Golubov, H. Trinkaus, A. Serra, Y.N. Osetsky, A.V. Barashev, Aspects of microstructure evolution under cascade damage conditions, *J. Nucl. Mater.* 251 (1997) 107–122, [https://doi.org/10.1016/S0022-3115\(97\)00244-4](https://doi.org/10.1016/S0022-3115(97)00244-4).
- [35] S. Hasanzadeh, R. Schaublin, B. Decamps, V. Rousson, E. Autissier, M.-F. Barthe, C. Hebert, Three-dimensional scanning transmission electron microscopy of dislocation loops in tungsten, *Micron* 113 (2018) 24–33, <https://doi.org/10.1016/j.micron.2018.05.010>.
- [36] G. Bonny, D. Terentyev, J. Elena, A. Zinovev, B. Minov, E. Zhurkin, Assessment of hardening due to dislocation loops in bcc iron: overview and analysis of atomistic simulations for edge dislocations, *J. Nucl. Mater.* 473 (2016) 283–289, <https://doi.org/10.1016/j.jnucmat.2016.02.031>.
- [37] T.D.L.D. Rubia, M.J. Caturla, E.A. Alonso, N. Soneda, M.D. Johnson, The primary damage state and its evolution over multiple length and time scales: recent atomic-scale computer simulation studies, *Radiat. Eff. Defect S.* 148 (1999) 95–126, <https://doi.org/10.1080/10420159908229089>.
- [38] S.V. Dmitriev, A.Y. Morkina, D.V. Tarov, G.R. Khalikova, D.U. Abdullina, P.S. Tatarinov, V.P. Tatarinov, A.S. Semenov, O.B. Naimark, A.V. Khokhlov, V.V. Stolyarov, Effect of repetitive high-density current pulses on plastic deformation of copper wires under stepwise loading, *Spec. Mech. Eng. Oper. Res.* 1 (2024) 27–43, <https://doi.org/10.31181/smeor1120243>.
- [39] D. Peckner, I.M. Bernstein, D. Peckner, *Handbook of Stainless Steels*, McGraw-Hill, T.H.E., New York, 1977.
- [40] C.M.F. Rae, R.C. Reed, The precipitation of topologically close-packed phases in rhenium-containing superalloys, *Acta Mater.* 49 (2001) 4113–4125, [https://doi.org/10.1016/S1359-6454\(01\)00265-8](https://doi.org/10.1016/S1359-6454(01)00265-8).
- [41] T. Hwang, A. Hasegawa, K. Tomura, N. Ebisawa, T. Toyama, Y. Nagai, M. Fukuda, T. Miyazawa, T. Tanaka, S. Nogami, Effect of neutron irradiation on rhenium cluster formation in tungsten and tungsten-rhenium alloys, *J. Nucl. Mater.* 507 (2018) 78–86, <https://doi.org/10.1016/j.jnucmat.2018.04.031>.
- [42] M. Klimenkov, U. Jäntschi, M. Rieth, H.C. Schneider, D.E.J. Armstrong, J. Gibson, S.G. Roberts, Effect of neutron irradiation on the microstructure of tungsten, *Nucl. Mater. Energy.* 9 (2016) 480–483, <https://doi.org/10.1016/j.nme.2016.09.010>.
- [43] R. Herschitz, D.N. Seidman, Radiation-induced precipitation in fast-neutron irradiated tungsten-rhenium alloys: an atom-probe field-ion microscope study, *Nucl. Inst. Methods Phys. Res. B.* 7–8 (1985) 137–142, [https://doi.org/10.1016/0168-583X\(85\)90544-0](https://doi.org/10.1016/0168-583X(85)90544-0).
- [44] A. Bakaev, A. Zinovev, D. Terentyev, G. Bonny, C. Yin, N. Castin, Y.A. Mastrikov, E.E. Zhurkin, Interaction of carbon with microstructural defects in a W-Re matrix: an ab initio assessment, *J. Appl. Phys.* 126 (2019) 075110, <https://doi.org/10.1063/1.5094441>.
- [45] P.M. Derlet, D. Nguyen-Manh, S.L. Dudarev, Multiscale modeling of crowdion and vacancy defects in body-centered-cubic transition metals, *Phys. Rev. B.* 76 (2007) 054107, <https://doi.org/10.1103/PhysRevB.76.054107>.
- [46] A. Bakaev, P. Grigorev, D. Terentyev, A. Bakaeva, E.E. Zhurkin, Y.A. Mastrikov, Trapping of hydrogen and helium at dislocations in tungsten: an ab initio study, *Nucl. Fusion* 57 (2017) 126040, <https://doi.org/10.1088/1741-4326/aa7965>.
- [47] H. Li, S. Wurster, C. Motz, L. Romaner, C. Ambrosch-Draxl, R. Pippan, Dislocation-core symmetry and slip planes in tungsten alloys: ab initio calculations and microcantilever bending experiments, *Acta Mater.* 60 (2012) 748–758, <https://doi.org/10.1016/j.actamat.2011.10.031>.
- [48] T. Tsuru, T. Suzudo, First-principles calculations of interaction between solutes and dislocations in tungsten, *Nucl. Mater. Energy.* 16 (2018) 221–225, <https://doi.org/10.1016/j.nme.2018.07.007>.
- [49] L. Romaner, C. Ambrosch-Draxl, R. Pippan, Effect of rhenium on the dislocation core structure in tungsten, *Phys. Rev. Lett.* 104 (2010) 195503, <https://doi.org/10.1103/PhysRevLett.104.195503>.
- [50] A. Vesti, P. Hiremath, S. Melin, P.A.T. Olsson, Ab-initio investigation of mechanical and fracture-related properties of W-Re σ and χ precipitates, *J. Nucl. Mater.* 577 (2023) 154261, <https://doi.org/10.1016/j.jnucmat.2023.154261>.
- [51] T. Tsuru, M. Wakeda, T. Suzudo, M. Itakura, S. Ogata, Anomalous solution softening by unique energy balance mediated by kink mechanism in tungsten-rhenium alloys, *J. Appl. Phys.* 127 (2020) 025101, <https://doi.org/10.1063/1.5131279>.
- [52] Y.-H. Li, H.-B. Zhou, L. Liang, N. Gao, H. Deng, F. Gao, G. Lu, G.-H. Lu, Transition from ductilizing to hardening in tungsten: the dependence on rhenium distribution, *Acta Mater.* 181 (2019) 110–123, <https://doi.org/10.1016/j.actamat.2019.09.035>.
- [53] Y. Chen, Y.-H. Li, N. Gao, H.-B. Zhou, W. Hu, G.-H. Lu, F. Gao, H. Deng, New interatomic potentials of W, Re and W-Re alloy for radiation defects, *J. Nucl. Mater.* 502 (2018) 141–153, <https://doi.org/10.1016/j.jnucmat.2018.01.059>.
- [54] Y.-H. Li, H.-B. Zhou, H. Deng, G. Lu, L. Hong, Towards understanding the mechanism of rhenium and osmium precipitation in tungsten and its implication for tungsten-based alloys, *J. Nucl. Mater.* 505 (2018) 30–43, <https://doi.org/10.1016/j.jnucmat.2018.03.035>.
- [55] Y.-W. You, X.-S. Kong, X. Wu, C. Liu, Q. Fang, J. Chen, G.-N. Luo, Clustering of transmutation elements tantalum, rhenium and osmium in tungsten in a fusion environment, *Nucl. Fusion* 57 (2017) 086006, <https://doi.org/10.1088/1741-4326/aa70b2>.
- [56] B. Xue, L. Bingchen, S. Jin, H.-B. Zhou, L. Liang, L. Hong, Phase-field modeling of the clustering of transmutation element rhenium in irradiated tungsten, *J. Nucl. Mater.* 566 (2022) 153810, <https://doi.org/10.1016/j.jnucmat.2022.153810>.
- [57] S. Starikov, V. Jamebozorgi, D. Smirnova, R. Drautz, M. Mrovec, Atomistic simulations of pipe diffusion in bcc transition metals, *Acta Mater.* 260 (2023) 119294, <https://doi.org/10.1016/j.actamat.2023.119294>.
- [58] B.-C. Xu, X.-C. Li, J. Wang, X. Zhao, Y.-W. Li, X.-D. Pan, H.-S. Zhou, G.-N. Luo, Atomic study of the trapped and migration patterns of point defects around screw dislocation in tungsten, *Nucl. Mater. Energy.* 34 (2023) 101400, <https://doi.org/10.1016/j.nme.2023.101400>.
- [59] P.-D. Lin, J.-F. Nie, Y.-P. Lu, C.-X. Shi, S.-G. Cui, W.-D. Cui, L. He, Atomic irradiation defects induced hardening model in irradiated tungsten based on molecular dynamics and CPFEM, *Int. J. Plast.* 174 (2024) 103895, <https://doi.org/10.1016/j.ijplas.2024.103895>.
- [60] T.-R. Yang, Y.-H. Li, Q.-Y. Ren, D. Terentyev, H.-X. Xie, N. Gao, H.-B. Zhou, F. Gao, G.-H. Lu, Influence of rhenium-decorated dislocation loops on edge dislocation gliding in tungsten, *Scr. Mater.* 235 (2023) 115624, <https://doi.org/10.1016/j.scriptamat.2023.115624>.
- [61] D. Terentyev, D.J. Bacon, Y.N. Osetsky, Interaction of an edge dislocation with voids in α -iron modelled with different interatomic potentials, *J. Condens. Matter. Phys.*

- 20 (2008) 445007, <https://doi.org/10.1016/10.1088/0953-8984/20/44/445007>.
- [62] N. Anento, A. Serra, Interaction of a mobile {112} grain boundary with radiation induced defects in α -Fe: transformation of defects and impact on the shear-coupled grain boundary migration, *Comp. Mater. Sci.* 179 (2020) 109679, <https://doi.org/10.1016/j.commatsci.2020.109679>.
- [63] N. Kvashin, P.L. Garcia-Muller, N. Anento, A. Serra, Atomic processes of shear-coupled migration in {112} twins and vicinal grain boundaries in bcc-Fe, *Phys. Rev. Mater.* 4 (2020) 073604, <https://doi.org/10.1103/PhysRevMaterials.4.073604>.
- [64] G. Monnet, D. Terentyev, Structure and mobility of the 1/2{111}{112} edge dislocation in bcc iron studied by molecular dynamics, *Acta Mater.* 57 (2009) 1416–1426, <https://doi.org/10.1016/j.actamat.2008.11.0310>.
- [65] A. Kazakov, R.I. Babicheva, A. Zinovev, D. Terentyev, K. Zhou, E.A. Korznikova, S.V. Dmitriev, Interaction of edge dislocations with voids in tungsten, *Tungsten* 6 (2023) 633–646, <https://doi.org/10.1007/s42864-023-00250-0>.
- [66] G. Bonny, A. Bakaev, D. Terentyev, Assessment of hardening due to noncoherent precipitates in tungsten-rhenium alloys at the atomic scale, *Sci. Rep.* 9 (2019) 16215, <https://doi.org/10.1038/s41598-019-52521-x>.
- [67] T. Tanno, A. Hasegawa, J.-C. He, M. Fujiwara, S. Nogami, M. Satou, T. Shishido, K. Abe, Effects of transmutation elements on neutron irradiation hardening of tungsten, *Mater. Trans.* 48 (2007) 2399–2402, <https://doi.org/10.2320/matertrans.MAW200722>.
- [68] Z. Zhang, K. Yabuuchi, A. K. Defect distribution in ion-irradiated pure tungsten at different temperatures, *J. Nucl. Mater.* 480 (2016) 207–215, <https://doi.org/10.1016/j.jnucmat.2016.08.029>.
- [69] Y.N. Osetsyki, D.J. Bacon, Atomic-scale mechanisms of void hardening in bcc and fcc metals, *Philos. Mag.* 90 (2010) 945–961, <https://doi.org/10.1080/14786430903164580>.
- [70] G. Pintsuk, A. Hasegawa, Tungsten as a plasma-facing material, in: R. Konings, R. Stoller, eds., *Comprehensive Nuclear Materials*, second ed., Elsevier, 2020, pp. 19–53, <https://doi.org/10.1016/B978-0-12-803581-8.11696-0>.
- [71] E. Lang, N. Reid, L. Garrison, C. Parish, J. Allain, Pre-irradiation comparison of W-based alloys for the PHENIX campaign: microstructure, composition, and mechanical properties, *Fusion Sci. Tech.* 75 (2019) 533–541, <https://doi.org/10.1080/15361055.2019.1602400>.
- [72] M.J. Lloyd, J. Haley, B. Jim, R. Abernethy, M.R. Gilbert, E. Martinez, K. Hattar, O. El-Atwani, D. Nguyen-Manh, M. Moody, P.A.J. Bagot, D.E.J. Armstrong, Microstructural evolution and transmutation in tungsten under ion and neutron irradiation, *Materialia* 33 (2024) 101991, <https://doi.org/10.1016/j.mtla.2023.101991>.
- [73] A.Y. Morkina, R.I. Babicheva, E.A. Korznikova, N.A. Enikeev, K. Edalati, S.V. Dmitriev, A molecular dynamics simulation to shed light on the mechanical alloying of an Al-Zr alloy induced by severe plastic deformation, *Metals* 13 (2023) 1595, <https://doi.org/10.3390/met13091595>.
- [74] D.S. Ryabov, G.M. Chechin, E.K. Naumov, Y.V. Bebikhov, E.A. Korznikova, S.V. Dmitriev, One-component delocalized nonlinear vibrational modes of square lattices, *Nonlinear. Dyn.* 111 (2023) 8135–8153, <https://doi.org/10.1007/s11071-023-08264-6>.
- [75] I.A. Shepelev, I.D. Kolesnikov, Excitation and propagation of 1-crowdion in bcc niobium lattice, *Mater. Technol. Des.* 8 (2022) 5–10, https://doi.org/10.54708/26587572_2022_4175.
- [76] U.I. Yankovskaya, P.V. Zakharov, Heat resistance of a Pt crystal reinforced with CNTs, *Mater. Technol. Des.* 3 (2021) 64–67, https://doi.org/10.54708/26587572_2021_34664.
- [77] A.V. Savin, E.A. Korznikova, S.V. Dmitriev, Simulation of folded and scrolled packings of carbon nanoribbons, *Phys. Solid State* 57 (2015) 2348–2355, <https://doi.org/10.1134/S1063783415110293>.
- [78] H. Chen, N. Tsou, The analysis of thermal-induced phase transformation and micro-structural evolution in Ni-Ti based shape memory alloys by molecular dynamics, *Comput. Model. Eng. Sci.* 120 (2019) 319–332, <https://doi.org/10.32604/cmescs.2019.06447>.
- [79] A.Y. Morkina, D.V. Bachurin, S.V. Dmitriev, A.S. Semenov, E.A. Korznikova, Modulational instability of delocalized modes in fcc copper, *Materials* 15 (2022) 5597, <https://doi.org/10.3390/ma15165597>.
- [80] I.D. Kolesnikov, S.A. Shcherbinin, Y.V. Bebikhov, E.A. Korznikova, I.A. Shepelev, A.A. Kudreyko, S.V. Dmitriev, Chaotic discrete breathers in bcc lattice, *Chaos. Solit. Fract.* 178 (2024) 114339, <https://doi.org/10.1016/j.chaos.2023.114339>.
- [81] R. Babicheva, A. Jarlov, H. Zheng, S. Dmitriev, E. Korznikova, M. Ling Sharon Nai, U. Ramamurty, K. Zhou, Effect of short-range ordering and grain boundary segregation on shear deformation of CoCrFeNi high-entropy alloys with Al addition, *Comp. Mater. Sci.* 215 (2022) 111762, <https://doi.org/10.1016/j.commatsci.2022.111762>.
- [82] S. Plimpton, Fast parallel algorithms for short-range molecular dynamics, *J. Comput. Phys.* 117 (1995) 1–19, <https://doi.org/10.1006/jcph.1995.1039>.
- [83] G. Bonny, A. Bakaev, D. Terentyev, Y.A. Mastrikov, Interatomic potential to study plastic deformation in tungsten-rhenium alloys, *J. Appl. Phys.* 121 (2017) 165107, <https://doi.org/10.1063/1.4982361>.
- [84] I.V. Kosarev, S.A. Shcherbinin, A.A. Kistanov, R.I. Babicheva, E.A. Korznikova, S.V. Dmitriev, An approach to evaluate the accuracy of interatomic potentials as applied to tungsten, *Comp. Mater. Sci.* 231 (2024) 112597, <https://doi.org/10.1016/j.commatsci.2023.112597>.
- [85] A. Stukowski, Visualization and analysis of atomistic simulation data with ovito—the open visualization tool, *Model. Simul. Mater. Sci. Eng.* 18 (2010) 015012, <https://doi.org/10.1088/0965-0393/18/1/015012>.
- [86] T. Tanno, M. Fukuda, S. Nogami, A. Hasegawa, Microstructure development in neutron irradiated tungsten alloys, *Mater. Trans.* 52 (2011) 1447–1451, <https://doi.org/10.2320/matertrans.MBW201025>.
- [87] B. Bryskin, J.-C. Carlen, Sigma phase in tungsten-rhenium alloys, *Mater. Manuf. Process.* 11 (1996) 67–81, <https://doi.org/10.1080/10426919608947461>.
- [88] G.A. Cottrell, Sigma phase formation in irradiated tungsten, tantalum and molybdenum in a fusion power plant, *J. Nucl. Mater.* 334 (2004) 166–168, <https://doi.org/10.1016/j.jnucmat.2004.07.001>.
- [89] M.C. Marinica, L. Ventelon, M.R. Gilbert, L. Proville, S.L. Dudarev, J. Marian, G. Bencteux, F. Willaime, Interatomic potentials for modelling radiation defects and dislocations in tungsten, *J. Condens. Matter. Phys.* 25 (2013) 395502, <https://doi.org/10.1088/0953-8984/25/39/395502>.
- [90] A.R. Khalikov, E.A. Korznikova, A.A. Kudreyko, Y.V. Bebikhov, S.V. Dmitriev, Planar superstructure defects in ordered alloys with L10 structure, *Metals Mater. Int.* 29 (2023) 1712–1722, <https://doi.org/10.1007/s12540-022-01321-6>.
- [91] D.J. Bacon, U.F. Kocks, R.O. Scattergood, The effect of dislocation self-interaction on the Orowan stress, *Philos. Mag.* 28 (1973) 1241–1263, <https://doi.org/10.1080/14786437308227997>.
- [92] E. Orowan, Discussion on internal stresses, in: *Symposium on Internal Stresses in Metals and Alloys*, Institute of Metals, London, UK, 1948, pp. 451–453.
- [93] V. Gerold, H.-M. Pham, Precipitation hardening by misfitting particles and its comparison with experiments, *Scr. Metall.* 13 (1979) 895–898, [https://doi.org/10.1016/0036-9748\(79\)90182-0](https://doi.org/10.1016/0036-9748(79)90182-0).
- [94] M. Shukeir, L. Dupuy, B. Devincs, Simulation of Orowan's mechanism using dislocation dynamics based on the non-singular elastic theory. (2020). <https://cea.hal.science/cea-02339875>.

- [95] S. Queyreau, G. Monnet, B. Devincere, Orowan strengthening and forest hardening superposition examined by dislocation dynamics simulations, *Acta Mater.* 58 (2010) 5586–5595, <https://doi.org/10.1016/j.actamat.2010.06.028>.
- [96] Z. Wang, Q. Li, S. Pang, X. Li, C. Dong, P. Liaw, Coherent precipitation and strengthening in compositionally complex alloys: a review, *Entropy* 20 (2018) 878, <https://doi.org/10.3390/e20110878>.
- [97] A. Melander, P. Persson, The strength of a precipitation hardened alznmg alloy, *Acta Metall* 26 (1978) 267–278, [https://doi.org/10.1016/0001-6160\(78\)90127-X](https://doi.org/10.1016/0001-6160(78)90127-X).
- [98] A. Ardell, Precipitation hardening, *Metall. Trans. A* 16 (1985) 2131–2165, <https://doi.org/10.1007/BF02670416>.
- [99] A. Stukowski, Structure identification methods for atomistic simulations of crystalline materials, *Model. Simul. Mater. Sci. Eng.* 20 (2012) 045021, <https://doi.org/10.1088/0965-0393/20/4/045021>.
- [100] A. Stukowski, V.V. Bulatov, A. Arsenlis, Automated identification and indexing of dislocations in crystal interfaces, *Model. Simul. Mater. Sci. Eng.* 20 (2012) 085007, <https://doi.org/10.1088/0965-0393/20/8/085007>.
- [101] Y. Osetsky, Strengthening of tungsten by coherent rhenium precipitates formed during low fluence irradiation, *Tungsten* 4 (2022) 20–27, <https://doi.org/10.1007/s42864-021-00088-4>.
- [102] A.P. Chetverikov, I.A. Shepelev, E.A. Korznikova, A.A. Kistanov, S.V. Dmitriev, M.G. Velarde, Breathing subsonic crowdion in Morse lattices, *Comput. Condens. Matter.* 13 (2017) 59–64, <https://doi.org/10.1016/j.cocom.2017.09.004>.
- [103] A. Moradi Marjaneh, D. Saadatmand, I. Evazzade, R.I. Babicheva, E.G. Soboleva, N. Srikanth, K. Zhou, E.A. Korznikova, S.V. Dmitriev, Mass transfer in the Frenkel-Kontorova chain initiated by molecule impact, *Phys. Rev. E* 98 (2018) 023003, <https://doi.org/10.1103/PhysRevE.98.023003>.
- [104] R.I. Babicheva, I. Evazzade, E.A. Korznikova, I.A. Shepelev, K. Zhou, S.V. Dmitriev, Low-energy channel for mass transfer in Pt crystal initiated by molecule impact, *Comput. Mater. Sci.* 163 (2019) 248–255, <https://doi.org/10.1016/j.commatsci.2019.03.022>.
- [105] I.A. Shepelev, S.V. Dmitriev, A.A. Kudreyko, M.G. Velarde, E.A. Korznikova, Supersonic voidions in 2D Morse lattice, *Chaos Solit. Fractals* 140 (2020) 110217, <https://doi.org/10.1016/j.chaos.2020.110217>.